



**HAL**  
open science

## Calibrating and scaling semi-empirical foam flow models for the assessment of foam-based EOR processes (in heterogeneous reservoirs)

O. Gassara, F. Douarche, B. Braconnier, B. Bourbiaux

### ► To cite this version:

O. Gassara, F. Douarche, B. Braconnier, B. Bourbiaux. Calibrating and scaling semi-empirical foam flow models for the assessment of foam-based EOR processes (in heterogeneous reservoirs). *Transport in Porous Media*, 2020, 131 (1), pp.193-221. 10.1007/s11242-018-01223-5 . hal-02571986

**HAL Id: hal-02571986**

**<https://ifp.hal.science/hal-02571986>**

Submitted on 13 May 2020

**HAL** is a multi-disciplinary open access archive for the deposit and dissemination of scientific research documents, whether they are published or not. The documents may come from teaching and research institutions in France or abroad, or from public or private research centers.

L'archive ouverte pluridisciplinaire **HAL**, est destinée au dépôt et à la diffusion de documents scientifiques de niveau recherche, publiés ou non, émanant des établissements d'enseignement et de recherche français ou étrangers, des laboratoires publics ou privés.

## Calibrating and scaling semi-empirical foam flow models for the assessment of foam-based EOR processes (in heterogeneous reservoirs)

O. Gassara, F. Douarche, B. Braconnier, B. Bourbiaux

Received: date / Accepted: date

**Abstract** Models for simulating foam-based displacements fall into two categories: population-balance (PB) models that derive explicitly foam texture or bubble size from pore-level mechanisms related to lamellas generation and coalescence, and steady-state semi-empirical (SE) models that account implicitly for foam texture effects through a gas mobility reduction factor. This mobility reduction factor has to be calibrated from a large number of experiments on a case by case basis in order to match the physical effect of parameters impacting foam flow behavior such as fluids saturation and velocity.

This paper proposes a methodology to set up steady-state SE models of foam flow on the basis of an equivalence between SE model and PB model under steady-state flow conditions. The underlying approach consists in linking foam mobility and foam lamellas density (or texture) data inferred from foam corefloods performed with different foam qualities and velocities on a series of sandstones of different permeabilities. Its advantages lie in a deterministic non-iterative transcription of flow measurements into texture data, and in a separation of texture effects and shear-thinning (velocity) effects.

Then, scaling of foam flow parameters with porous medium permeability is established from the analysis of calibrated foam model parameters on cores of different permeability, with the help of theoretical representations of foam flow in a confined medium. Although they remain to be further confirmed from other well-documented experimental data sets, the significance of those scaling laws is great for the assessment of foam-based enhanced oil recovery (EOR) processes because foam EOR addresses heterogeneous reservoirs. Simulations of foam displacement in a reservoir cross-section demonstrate the necessity to scale foam SE models with respect to facies heterogeneity for reliable evaluation.

**Keywords** Multiphase flow · Porous media · Foam · Scaling laws · Heterogeneity · Models · Reservoir simulation · Reservoir engineering · Enhanced oil recovery

---

O. Gassara, F. Douarche, B. Bourbiaux,  
IFP Energies nouvelles, Geosciences Division, 1 et 4 avenue de Bois-Préau, 92852 Rueil-Malmaison Cedex,  
France,  
E-mail: frederic.douarche@ifpen.fr, bernard.bourbiaux@ifpen.fr

B. Braconnier,  
IFP Energies nouvelles, Mechatronics and Numerics Division, 1 et 4 avenue de Bois-Préau, 92852 Rueil-  
Malmaison Cedex, France,  
E-mail: benjamin.braconnier@ifpen.fr

## 1 Introduction

Since the sixties, foam-drive processes have been considered as a promising enhanced oil recovery (EOR) technique [1,2,3,4,5]. Indeed, the injection of foam instead of gas alleviates gravity override and detrimental effects of heterogeneities and viscous instabilities on displacement efficiency.

Foam in porous media is defined as a dispersion of gas in liquid carrying surfactants [6], such that at least a fraction of the gas phase is discontinuous and the liquid phase is continuous and connected through wetting films and lamellas separating gas bubbles. Surfactants in foam context are used to stabilize the thin liquid lamellas and promote the foaming ability of the mixture. Foam is usually characterized by its texture, defined as the number of foam bubbles or lamellas per unit volume of gas, and also its quality  $f_g$  which is the ratio between the volumetric flux of foamed-gas and the total volumetric flux of gas and liquid.

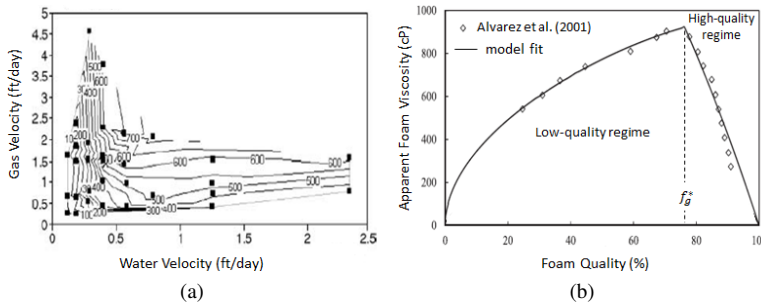


Fig. 1: (a) Contours of iso-steady-state pressure gradient as a function of gas and liquid velocities: vertical and horizontal contours represent the high- and low-quality regimes, respectively (adapted from [7]); (b) Apparent foam viscosity for a single scan of foam quality at constant total velocity (adapted from [8]).

Foam reduces gas mobility compared to gas flowing as a continuous phase, whereas the mobility of liquid phase is presumed to remain unchanged [9, 10, 11]. This reduced gas mobility can be seen as an increased effective gas viscosity, a decreased gas relative permeability, or also as a combination of the two effects [12, 13, 6, 14]. Rheological properties of foam are complicated since they depend on several parameters such as foam texture, which is the result of several pore-level scale mechanisms of lamellas generation and destruction, gas and liquid velocities (foam behaves as a shear-thinning fluid in porous media), permeability and porosity of the porous medium, surfactant formulation and concentration.

Coarsely-textured foams are characterized by a small number of lamellas and are referred to as weak foams since they provide a moderate gas mobility reduction, whereas finely-textured foams, called strong foams, are characterized by a large number of lamellas and reduce gas mobility remarkably. The transition from weak foam to strong foam state is called foam generation which is usually thought to be governed by pressure gradient (or equivalently total velocity) [15, 16, 17, 18].

The strong foam resulting from that generation process exhibits two different regimes: the low-quality regime, at which the steady-state pressure gradient is almost independent of water flow rate, and the high-quality regime at which the pressure gradient is nearly independent of gas velocity. These two regimes were first highlighted by Osterloh and Jante

[19] and later on by Alvarez et al [7] who represented the iso-value contours of the steady-state pressure gradient of strong foam as a function of gas and liquid volumetric fluxes as shown in Fig. 1(a). As any straight line drawn from the origin in this diagram represents a fixed foam quality, one can identify a specific value, called the optimal foam quality  $f_g^*$ , that divides the domain into two parts and provides the maximum pressure gradient that can be obtained for any given value of the total velocity. One can also clearly identify these two regimes from the evolution of the apparent foam viscosity  $\mu_f$  with foam quality at constant total velocity, as reported in Fig. 1(b).  $\mu_f$  is directly inferred from the pressure gradient  $\nabla P$  by application of Darcy's law to foam considered as a single homogenous phase, that is  $\mu_f = k|\nabla P|/u$ , where  $k$  is the permeability of the porous medium and  $u$  the total velocity. In the low-quality regime,  $\mu_f$  (or  $\nabla P$ ) increases with foam quality  $f_g$  until the optimal foam quality  $f_g^*$  for which the maximum value of the apparent foam viscosity is reached. For foam qualities higher than  $f_g^*$ , lamellas rupture occurs and  $\mu_f$  (or  $\nabla P$ ) decreases, as reported in Fig. 1(a).

The two strong-foam regimes are dominated by different mechanisms: the low-quality regime is characterized by the mobilization of foam bubbles in proportion to foam quality (a fixed bubble size is assumed), and the high-quality regime is characterized by lamellas coalescence as the liquid films in this regime become unstable. By conducting foam flow experiments in beadpacks, Khatib et al [20] found that the transition between these two regimes corresponds to a maximum or critical gas-liquid capillary pressure, denoted  $P_c^*$ , above which foam collapses (see Fig. 2). Since capillary pressure is related to water saturation, there is a critical (or limiting) water saturation  $S_w^*$  corresponding to  $P_c^*$ . It has been shown that the magnitude of  $P_c^*$ , or equivalently  $S_w^*$ , varies with surfactant concentration, electrolyte concentration, gas flow rate and permeability [20]. The dependence of  $P_c^*$  on the permeability is not yet clearly elucidated. Nonetheless, predicting the evolution of foam apparent viscosity with the permeability of the porous medium is of primary importance in evaluating foam process at the scale of a reservoir with permeability heterogeneities.

A variety of models has been proposed for modelling foam flow in porous media, which can be classified into two main groups. The first group includes population-balance (PB) models that account for pore-level mechanisms related to lamella creation and coalescence in order to track the dynamical behavior of foam texture in porous media along with its effect on gas mobility [13, 11, 22, 23]. Alternatively, a local steady-state version of PB models [22, 23, 24] comes out by equating the lamella creation and coalescence rates; solving this equation yields the foam texture. Semi-empirical (SE) models, that constitute the second group, assume that an equilibrium state is attained instantaneously such that the foam texture effects can be represented implicitly through a gas mobility reduction factor that depends on fluid saturation, interstitial velocity, surfactant concentration and other factors [25, 26]. SE models incorporate implicitly the limiting capillary pressure with a steep transition function which represents the coalescence effects on the mobility reduction factor. This mobility reduction factor has to be calibrated from a large number of experiments on a case by case basis in order to match the physical effect of each considered parameter on foam behavior.

Thus, this paper is organized as follows. Foam flow modelling in porous media is introduced with a description of PB and SE models features and differences. Then, a formal equivalence between SE model and an example of PB model at steady state [27] (Kam et al., 2007) is established. Extensive discussion of SE and PB models equivalence and identification at steady state can be found in [28]. Based on that equivalence, a methodology to calibrate a foam SE model from experimental apparent foam viscosity data is detailed, starting with relative permeability data acquisition and going on with foam SE model calibration itself. Distinctive features of the methodology compared to usual calibrating procedures [8,

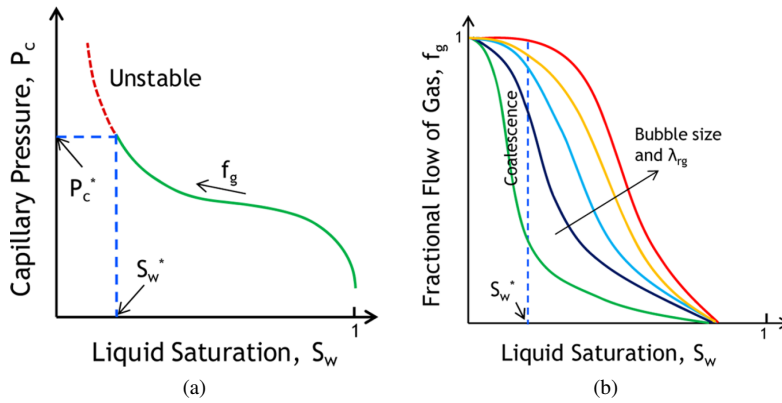


Fig. 2: Limiting capillary pressure schematics [20,21]. (a) Capillary pressure as a function of water saturation: capillary pressure increases with the gas saturation up to  $P_c^*$ , above which foam lamellas become unstable and coalesce; (b) Fractional flow of gas as a function of water saturation and bubble size: when water saturation reaches  $S_w^*$  corresponding to  $P_c^*$ , foam becomes coarser, gas fractional flow increases and consequently gas mobility increases. At low-quality regime, for  $S_w > S_w^*$ , the fractional flow of gas follows the green curve, then a transition occurs at  $S_w = S_w^*$  (dotted line), and finally the fractional flow of gas follows the red curve at high-quality regime for  $S_w < S_w^*$ .

29,30,31,21] include (a) the determination of a relation between foamed-gas viscosity and foam texture [12,32] thanks to a deterministic processing of experimental apparent viscosity data, and (b) the sequential calibration of shear-thinning effects and texture effects. Next, the methodology is implemented to parameterize the SE model of foam flow data measured on three cores of different permeabilities. Another section is dedicated to the analysis of calibrated parameters evolution with core permeability according to different assumptions regarding lamellas stability, in order to elucidate scaling laws of SE model parameters in the context of heterogeneous reservoirs. The implementation of that calibration methodology and the scaling of SE model parameters are also described with some additional details in [33]. Finally, the calibrated SE model including scaling laws is used to simulate foam flooding in a simplified heterogeneous reservoir cross-section, whereby demonstrating the significance of scaling issues for foam EOR assessment. Conclusions underline the main outcomes of this research study and remaining issues to be considered for a higher representativeness of foam models.

## 2 Foam modelling in porous media

In this section, we detail the two main types of models that describe foam flow in porous media, namely the population-balance (PB) models and the semi-empirical (SE) models. These models are based on the generalized Darcy approach that describes three-phase flows in usual reservoir simulators. Thus, for these models, foam is not modeled as an additional phase, but as a mixture of two water and gas phases. The foamed-gas phase mobility is modified whereas the liquid phase mobility remains unchanged [9,10,11]. However, both models require to model a surfactant which is needed for the foam or lamellas formation

and stability. Before underlining the PB and SE models specific features regarding gas mobility, we present the material balance equations for the water, hydrocarbon and surfactant components that underlie both types of model.

## 2.1 Common basic equations underlying PB and SE models

We consider a model for a three-phase flow in a porous medium in the presence of foam. We distinguish three phases: an aqueous phase  $w$ , an oil phase  $o$  and a gas phase  $g$ . This flow is modified by the presence of foam. Modelling foam requires the presence of a surfactant, which is transported by the water phase, and which requires to solve an additional mass balance equation. The surfactant is either mobile or adsorbed on the rock. When present in the water phase, we assume that the surfactant mass does not affect the water mass.

It has been shown [9, 10, 11] that the transport of liquid is not affected by the presence of foam. On the opposite, the gas velocity is significantly reduced by the presence of foam. Thus, to describe the water and hydrocarbon phases, we consider a black-oil model [34, 35] where the gas phase involves a modified velocity which will be denoted  $\mathbf{u}_g^f$ .

In the following, mass balance and flow equations are written in algebraic form because they will be applied to macroscopic 1D flow through porous medium cores. In 3D flow conditions however, anisotropic porous medium flow properties have to be considered. Then, the mass conservation equations read:

$$\begin{cases} \partial_t(\Phi\rho_w S_w) + \nabla \cdot (\rho_w \mathbf{u}_w) = q_w, \\ \partial_t(\Phi\rho_w S_w C_w^s + (1 - \Phi)\rho_r C_r^s) + \nabla \cdot (\rho_w \mathbf{u}_w C_w^s) = q_w C_w^s, \\ \partial_t(\Phi C_h \rho_o S_o) + \nabla \cdot (\rho_o C_h \mathbf{u}_o) = C_h q_o, \\ \partial_t(\Phi\rho_g S_g + \Phi C_v \rho_o S_o) + \nabla \cdot (\rho_o C_v \mathbf{u}_o + \rho_g \mathbf{u}_g^f) = q_g + C_v q_o, \end{cases} \quad (1)$$

where  $\Phi$  is the rock porosity. For each phase denoted  $\psi = w, o, g$ ,  $S_\psi$  is the saturation,  $\rho_\psi$  the density and  $q_\psi$  the source/sink term per unit volume of porous medium. The gas phase contains a single volatile component denoted  $v$ , whereas the oil phase contains a heavy component denoted  $h$  and previous volatile component  $v$ , with  $C_h$  and  $C_v = 1 - C_h$  their respective mass fraction (in the oil phase). The equilibrium constant  $K_v = \frac{1}{X_v}$ , with  $X_v$  the molar fraction of volatile component in the oil phase, is defined from molar masses of  $v$  and  $h$ , and mass fractions  $C_v$  and  $C_h$ .  $K_v$  is a function of pressure.  $C_w^s$  stands for the flowing surfactant mass fraction in the water phase and  $C_r^s$  for the adsorbed surfactant mass fraction on the rock with  $\rho_r$  the rock mass density. Mobile and adsorbed surfactant mass fractions are related with an adsorption law such as the Langmuir isotherm [36, 37].

Under creeping (i.e. low-velocity) flow conditions, the pure phase velocities in permeable porous media are governed by the generalized Darcy's law:

$$\mathbf{u}_\psi = -\frac{k k_{r\psi}}{\mu_\psi} (\nabla P_\psi - \rho_\psi \mathbf{g}), \quad (2)$$

where  $k$  is the rock permeability,  $\mu_\psi$  the pure phase viscosity,  $P_\psi$  the pressure of the phase  $\psi$  and  $\mathbf{g}$  the gravity acceleration.  $k_{r\psi}$  is the relative permeability for the pure phase  $\psi$ , i.e. without lamellas. We suppose the relative permeabilities and capillary pressure functions are known, with given saturation end points. In our specific context of foam modelling, we will only consider the gas and water phases, thus  $S_g \in [S_{gr}, 1 - S_{wi}]$  where  $S_{gr}$  is the residual gas saturation and  $S_{wi}$  the irreducible water saturation.

In order to simplify the notations in the following, we introduce the phase mobility  $\lambda_\psi = k_{r,\psi}/\mu_\psi$  and the interstitial velocity  $\mathbf{v}_\psi = \mathbf{u}_\psi/(\Phi S_\psi)$  (see [38] for more details). We also introduce the phase fractional flow  $f_\psi = |\mathbf{u}_\psi|/|\mathbf{u}|$  where the total velocity  $\mathbf{u} = \sum_{\psi \in \{w,o,g\}} \mathbf{u}_\psi$  is the sum of the phase velocities.

The flow of gas in the presence of foam is discussed later on as it is modeled differently whether a population-balance or a semi-empirical modelling approach is used. These models are based on Darcy-type laws which are extended to obtain a modified gas velocity which is detailed for the PB and SE models in the two next sections respectively.

## 2.2 Population-balance lamellas models

Foam mobility is strongly related to its texture which is a key variable in foam modelling in porous media: as foam texture increases, the resistance to gas flow in porous media increases. Population-balance models were designed in order to relate explicitly the gas mobility reduction to the foam texture. Thus, for PB models, the dynamics of foam texture needs to be modeled and a lamella population-balance equation is considered. The impact of foam texture on gas mobility is modeled through an effective gas viscosity and a gas trapping for more elaborated models [11, 24, 6]. In this study, we focus on viscosity-type PB models and do not consider gas trapping.

The population-balance model involves a lamellas balance that includes lamellas advection at the modified gas velocity and source/sink terms taking into account lamellas creation and destruction [39, 13]. The lamellas population balance equation reads:

$$\partial_t(\Phi S_g n_f) + \nabla \cdot (\mathbf{u}_g n_f) = \Phi S_g (r_g - r_c) + q_f, \quad (3)$$

where  $n_f$  is the foam texture, that is the number of flowing lamellas (or foam bubbles) per unit volume of gas and  $q_f$  is the external lamellas source/sink term (number of lamellas per unit of time and per unit volume of porous medium).

As mentioned earlier, the gas velocity is significantly reduced when foam develops. The viscosity-type PB models extend the generalized Darcy's equation for the gas phase as follows:

$$\mathbf{u}_g = -\frac{kk_{rg}}{\mu_g^{\text{PB}}} (\nabla P_g - \rho_g \mathbf{g}), \quad (4)$$

where  $\mu_g^{\text{PB}}$  is the effective gas viscosity when flowing as a succession of bubbles. The rheology of PB models of foam flow is classically based on Bretherton's flow model of a single bubble within a capillary [32], that was later extended by Hirasaki and co-workers to a train of bubbles [12] thus leading to the following expression for the effective gas viscosity:

$$\mu_g^{\text{PB}} = \mu_g + \frac{c_f n_f}{|\mathbf{v}_g|^{1/3}}, \quad (5)$$

where  $\mathbf{v}_g$  is the interstitial gas velocity in the presence of foam, deduced from  $\mathbf{u}_g$ .  $c_f$  is a constant depending on the surfactant concentration and the permeability of the porous medium [23].

The velocity power function involved in the expression of  $\mu_g^{\text{PB}}$  expresses the shear-thinning effect of flow on foam bubbles. The value of the exponent,  $\frac{1}{3}$ , was determined by Bretherton for the motion of a single bubble in a capillary tube with smooth walls [32]. However, for so complex pore geometries as natural porous media, the shear-thinning effect cannot be modelled with the same power function as will be shown later on.

$r_g$  and  $r_c$  are the rates of lamellas creation and coalescence. Different formulas have been proposed in the PB models of the literature to model these rates [6,27,40]. For the purpose of our paper, we propose to focus on the Kam et al [27] model for which the creation and coalescence rates read:

$$r_g = c_g S_w |\nabla P_g|^m \quad \text{and} \quad r_c = \frac{c_c n_f}{(S_w - S_w^{*-PB})^n}, \quad (6)$$

where  $c_g$  is the generation rate coefficient,  $c_c$  the coalescence rate coefficient,  $n$  a coalescence exponent,  $m$  a model parameter, and where the foam texture  $n_f$  cannot exceed a maximum value  $n_f^{\max}$ .

The formulations of these rates need to be commented. Regarding lamellas generation, Kam et al [27] suggested that the rate of lamellas creation in porous media is proportional to the water saturation and to a power-law expression of the gas-phase pressure gradient. Specifically, foam generation is easier at higher water saturation because more liquid lenses can be generated within the pore network. Regarding lamellas coalescence, the rate  $r_c$  is expressed as a function of the foam texture  $n_f$  and the limiting water saturation  $S_w^{*-PB}$ , corresponding to the limiting capillary pressure  $P_c^*$ . The expression of  $r_c$  predicts a destruction of all lamellas as  $S_w$  approaches  $S_w^{*-PB}$ .

The population balance model is at steady state when rates of foam generation and coalescence are equal. This equality between  $r_g$  and  $r_c$  can be used to link the foam texture to the water saturation as detailed in [28].

As regards the foam texture in a porous medium, it is acknowledged that the size of foam bubbles (that is the inverse of  $n_f$ ) is closely depending on the pore structure [13,11]. In first approximation, it can be estimated as the volume of spherical bubbles with a radius  $r$  in the order of characteristic pore radius, the latter being a function of porous medium flow properties [23]. Following Alvarez et al's working hypothesis [7], Kam et al [27] assume that the size of individual foam bubbles is constant in the low-quality regime once the conditions of foam generation (velocity) are met, then increases in the high-quality regime because of coalescence. To end with, according to Kam et al model, the maximum foam texture  $n_f^{\max}$  is obtained in the low-quality regime and can be estimated from a characteristic pore radius. However, that question of foam texture remains controversial because the mechanisms of lamellas generation are complex [6] and hardly tractable in the context of natural porous media, but such a discussion is beyond the scope of present work.

Overall, expressions (6) incorporate the qualitative physical trends of foam texture dependence on the porous medium as discussed above, but they still have to be calibrated from experiments, such as the ones from Alvarez et al [7] and Moradi-Araghi et al [41].

### 2.3 Semi-empirical foam models

Most semi-empirical (SE) foam flow simulators apply a gas mobility reduction factor when surfactant is present in the water phase. More precisely, the gas mobility  $\lambda_g^{\text{SE}}$  of SE model is scaled by a multi-parameter interpolation function  $FM$  assigned to the relative permeability to gas, whereas the gas viscosity is assumed unchanged whether foam is present or not:

$$\mathbf{u}_g = -k\lambda_g^{\text{SE}} (\nabla P_g - \rho_g \mathbf{g}) \quad \text{with} \quad \lambda_g^{\text{SE}} = \frac{k_{rg}^{\text{SE}}}{\mu_g} = \frac{FM \cdot k_{rg}}{\mu_g}, \quad (7)$$

where  $k_{rg}^{SE}$  is the modified gas relative permeability for the SE model in the presence of foam and  $k_{rg}$  is the conventional relative permeability of gas.  $FM$  is a multi-parameter interpolation functional form that includes the contributions of physical parameters impacting the gas mobility reduction.  $FM$  is formulated as follows:

$$FM = \frac{1}{1 + (M_{ref} - 1) \prod_{i=1}^4 F_i}, \quad (8)$$

where  $M_{ref}$  is the reference (maximum) gas mobility reduction under optimal conditions of the rock-fluid-additive system under consideration, and  $F_i$  are functions of four physical parameters that are surfactant concentration, water saturation, oil saturation, and gas velocity, or equivalently, the gas capillary number. In this paper, we study the effect of water saturation and gas velocity on foam performance. Thus, we focus on the so called dry-out function  $F_2$  and shear-thinning function  $F_4$  ( $F_1$  and  $F_3$  functions account for surfactant concentration and oil saturation effects on foam performance, and are not developed herein). In our model,  $F_2$  reads:

$$F_2(S_w) = \frac{1}{2} + \frac{1}{\pi} \arctan [\Theta (S_w - S_w^*)], \quad (9)$$

where the dimensionless constant  $\Theta$  governs the sharpness of the transition from the low-quality regime to the high-quality regime as water saturation decreases in the vicinity of  $S_w^*$ . A very high value of  $\Theta$  (several thousands) leads to a steep transition and in this case foam coalescence occurs at the given water saturation  $S_w^*$ , whereas a low value (less than 100 or 10) yields a smooth transition in the vicinity of  $S_w^*$ .

Furthermore,  $FM$  includes a shear-thinning function  $F_4$  expressing the non-Newtonian behavior of foam flow in porous media: at fixed surfactant concentration and fluids saturations, foam mobility increases [32, 12, 13, 11]. That shear-thinning effect is assumed to follow a power function of interstitial gas velocity as found by Bretherton for bubble motion in a capillary. Hence,  $F_4$  can be expressed as:

$$F_4(|\mathbf{v}_g|) = \left( \frac{v_g^{ref}}{|\mathbf{v}_g|} \right)^{e_c}. \quad (10)$$

In SE models, that function is expressed as a function of capillary number  $N_{cg}$ , the dimensionless ratio between viscous and capillary forces. That is,  $F_4$  is formulated as:

$$F_4(N_{cg}) = \left( \frac{N_{cg}^{ref}}{N_{cg}} \right)^{e_c} \quad \text{with} \quad N_{cg} = \frac{\mu_g |\mathbf{u}_g|}{\Phi \sigma S_g}, \quad (11)$$

where  $N_{cg}^{ref}$  is a reference capillary number for which  $M_{ref}$  is measured,  $e_c$  is the exponent that drives the shear-thinning behavior and  $\sigma$  is the interfacial tension between gas and water. Shear-thinning behavior can be ignored by setting  $e_c = 0$ .

### 3 Identification of SE and PB models at local steady state

As only local steady state foam flow is modeled by SE model, the identification procedure developed hereafter will involve only the solutions of PB models at local equilibrium. As explained in the previous section, the gas-phase mobility  $\lambda_g^{PB}$  in most PB models is based on a modified gas viscosity whereas the foam mobility  $\lambda_g^{SE}$  in SE models is based on a

modified relative permeability of gas. Hence, the identification of SE-model gas mobility to PB-model gas mobility is  $\lambda_g^{\text{SE}} = \lambda_g^{\text{PB}}$ , that is  $k_{rg}^{\text{SE}}/\mu_g = k_{rg}^{\text{PB}}/\mu_g^{\text{PB}}$ :

$$(M_{\text{ref}} - 1) \prod_{i=1}^4 F_i = \frac{c_f n_f}{\mu_g |\mathbf{v}_g|^c}. \quad (12)$$

Note that the value of velocity exponent in Eq. 5 is now denoted  $c$  since the shear-thinning effect in a natural porous medium differs from that in a capillary tube, although qualitatively similar.

Assuming no oil and optimal concentration of foaming additive, the  $\prod_{i=1}^4 F_i$  product only involves the dry-out and shear-thinning functions  $F_2$  and  $F_4$  given by Eq. 9 and Eq. 11. In order to go further with the identification,  $F_4$  expression as a function of the interstitial velocity given by Eq. 10 is introduced in previous equation, which yields:

$$(M_{\text{ref}} - 1) F_2 \left( \frac{v_g^{\text{ref}}}{|\mathbf{v}_g|} \right)^{e_c} = \frac{c_f n_f}{\mu_g (v_g^{\text{ref}})^c} \left( \frac{v_g^{\text{ref}}}{|\mathbf{v}_g|} \right)^c. \quad (13)$$

The two members of that equation involve the same gas velocity variable, but saturation on the left hand, and texture on the right hand.

The dry-out function  $F_2$  models the foam texture decrease (decreasing number of lamellas per unit volume of gas) when a coalescence of foam bubbles occurs within the porous medium because of capillary pressure effects [21,29,31] taking place in the HQR (High Quality Regime). In the LQR (Low Quality Regime), foam texture (i.e. the number of lamellas per unit volume of gas) is assumed invariant and determined by the characteristic pore size of the porous medium. Therefore,  $F_2$  is constant as well as  $n_f$  in the LQR, which allows to identify the velocity-dependent terms of previous equation that is  $e_c = c$ .

To go further on with  $F_2$  identification, we note that the remaining variable in the right hand side of Eq. 13 is  $n_f$ , and that  $F_2$  function is scaled between 0 and 1. Therefore,  $F_2$  can be identified as:

$$F_2 = A n_f, \quad (14)$$

where  $A$  is a constant. Keeping in mind that  $n_f$  varies from 0 to  $n_f^{\text{max}}$ , the constant  $A$  can be fixed to  $1/n_f^{\text{max}}$  leading to:

$$F_2 = \frac{n_f}{n_f^{\text{max}}}. \quad (15)$$

To end up with the identification of SE model empirical parameters to PB model, we rewrite Eq. 13 as:

$$(M_{\text{ref}} - 1) F_2 \left( \frac{v_g^{\text{ref}}}{|\mathbf{v}_g|} \right)^c = \frac{c_f n_f^{\text{max}}}{\mu_g (v_g^{\text{ref}})^c} \frac{n_f}{n_f^{\text{max}}} \left( \frac{v_g^{\text{ref}}}{|\mathbf{v}_g|} \right)^c. \quad (16)$$

and infer the value of mobility reduction factor  $M_{\text{ref}}$ :

$$M_{\text{ref}} = 1 + \frac{c_f n_f^{\text{max}}}{\mu_g (v_g^{\text{ref}})^c}. \quad (17)$$

Identification summary is then:

$$M_{\text{ref}} = 1 + \frac{c_f n_f^{\text{max}}}{\mu_g (v_g^{\text{ref}})^c}, \quad F_2 = \frac{n_f}{n_f^{\text{max}}}, \quad F_4 = \left( \frac{v_g^{\text{ref}}}{|\mathbf{v}_g|} \right)^c. \quad (18)$$

To proceed with the identification of an SE model using the results of the above identification, we need to know the foam texture  $n_f$  for various foam flow conditions. This is provided by the solution of PB models at local steady state which is detailed hereafter.

#### 4 Methodology to calibrate a SE model from steady-state foam coreflood data

Foam coreflood experiments are generally performed for different values of the foam quality and different flow velocities in order to calibrate the  $F_2$  and  $F_4$  function. The effect of oil presence on mobility reduction performance is also studied from the confrontation of foam corefloods in the presence and in the absence of oil. For a core of given petrophysical properties, experimental data generally consist of foam apparent viscosity values measured at steady state for a set of quality values and of foam velocity values.

Herein, we focus on the calibration of  $F_2$  and  $F_4$  functions that drive foam mobility reduction performance. The method of calibration detailed hereafter and schematized in Fig. 3 is based on the previous equivalence established between SE model and PB model with texture as variable. That equivalence makes possible a calibration of  $F_4$  and  $F_2$  functions and of  $M_{\text{ref}}$ , provided that coreflood results are converted to texture values.

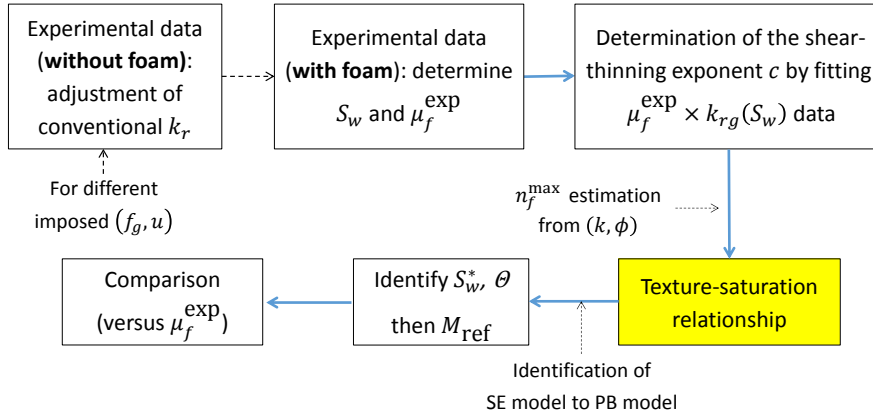


Fig. 3: Overview of the calibration methodology.

##### 4.1 Linking saturation and texture under steady-state flow conditions

For given quality and velocity of foam, the relationship between gas or liquid saturation and foam texture is obtained by introducing the rheological equation of foam, i.e. the expression of  $\mu_g^{\text{PB}}$  given by Eq. 5 into the gas-to-water fractional flow ratio  $\frac{f_g}{f_w}$ , written as  $\frac{k_{rg}}{k_{rw}} \frac{\mu_w}{\mu_g^{\text{PB}}}$  according to generalized Darcy's equations under the assumption of negligible capillary effects. After rearranging the terms, we obtain:

$$c_f n_f = \left( \frac{1 - f_g \frac{k_{rg}(S_w)}{k_{rw}(S_w)} \mu_w - \mu_g}{f_g} \right) \left( \frac{f_g u}{\Phi S_g} \right)^c. \quad (19)$$

That equation ties saturation to texture. Therefore, for a given value of foam quality  $f_g$  and of total velocity  $u$ ,  $n_f$  is known if saturation can be determined. This is possible because the water mobility is assumed unchanged whether gas is flowing as a continuous phase or as a foam. Water saturation is then determined by inverting the  $k_{rw}$  function for the value of  $k_{rw}$

calculated from generalized Darcy's equation with flow data at steady state.  $S_w$  derivation from foam apparent viscosity data is detailed in Appendix A.

Finally, a single value of foam texture  $n_f$  can be determined for any value of foam quality and of total velocity. In view of the independence of the parameter  $c_f$  on foam flow parameters, one can calculate the dimensionless foam texture values  $n_D$  for any experiment at given foam quality  $f_g$  and of total velocity  $u$ :

$$n_D(f_g, u) = \frac{c_f n_f(f_g, u)}{\max_i c_f n_f(f_g^i, u^i)}. \quad (20)$$

Determining  $n_f$  and constant  $c_f$  separately is not necessary because  $F_2$  is simply a scaled value of product  $c_f n_f$  determined as above. However, a value of  $c_f$  can be estimated from the maximum value of the product  $c_f n_f$  which is, in this case, equal to  $c_f n_f^{\max}$ , where  $n_f^{\max}$  is the reference foam texture value. That leads to:

$$n_D(f_g, u) = \frac{c_f n_f(f_g, u)}{c_f n_f^{\max}}. \quad (21)$$

$n_f^{\max}$  is correlated to the average pore radius  $r$  of the porous medium under consideration which is estimated in [42] as:

$$r = \sqrt{8k/\Phi}, \quad (22)$$

following the simplified representation of the porous medium as a bundle of identical capillary tubes of radius  $r$ .  $n_f^{\max}$  definition has to be specified further. Indeed, the pressure gradient due to foam flow is related to the number of lamellas per unit length in the flow direction under consideration, therefore the foam texture to be considered in Eq. 5 is a lineic texture, i.e. the number of lamellas per flow-length unit, denoted  $n_L$ . Then, considering foam bubbles as spheres of radius equal (or proportional) to pore radius  $r$ , the number of lamellas per unit flow length within pores of radius  $r$  is equal to:

$$n_L = \frac{\pi r^2}{\frac{4}{3}\pi(\lambda r)^3} = \frac{3}{4\lambda^3 r} \sim \frac{1}{r}, \quad (23)$$

where  $\lambda$  is a proportionality constant between the bubble radius and the pore radius. For model calibration developed later on,  $\lambda$  will be arbitrarily taken equal to 1, corresponding to spherical bubbles of radius  $r$ . Finally,  $n_f^{\max}$  in Eq. 21 should be replaced by  $n_L^{\max}$  that is the lineic texture quantified as:

$$n_L^{\max} = \frac{3}{4} \sqrt{\frac{\Phi}{8k}}. \quad (24)$$

## 4.2 Calibration of $F_4$ function

That calibration consists in the determination of the shear-thinning exponent  $c$ . This is possible in the LQR because the foam texture (i.e. the number of lamellas per unit volume of gas) is assumed invariant in that regime. Hence  $n_D(S_w)$  (i.e.  $F_2$  function) is assumed constant for any foam quality and velocity in the LQR. The  $F_4$  function exponent is then calibrated as follows. For a given foam quality, gas velocity can be expressed either as a function of apparent foam viscosity as  $u_g = f_g u = f_g \frac{k}{\mu_f} |\nabla P|$ , or from the generalized Darcy's law for

gas as  $u_g = \frac{kk_{rg}}{\mu_g^{\text{PB}}} |\nabla P|$ , with  $\mu_g^{\text{PB}}$  the foam gas viscosity from Eq. 5. Equality between both expressions leads to:

$$\mu_f k_{rg} = f_g \mu_g^{\text{PB}}.$$

We neglect the contribution of gas viscosity  $\mu_g$  in the expression of  $\mu_g^{\text{PB}}$  versus foam texture from Eq. 5 with exponent  $\frac{1}{3}$  replaced by  $c$ . This leads to:

$$\mu_f k_{rg} \approx f_g \frac{c_f n_f}{(v_g)^c}.$$

That expression shows that for foam flow experiments at fixed quality  $f_g$  and for fixed  $n_f$  value (i.e. within the LQR), the product of apparent foam viscosity and gas relative permeability is inversely proportional to the power function of gas phase velocity or of gas capillary number. Thus, for a set of experiments at different velocities with a given foam quality, the value of shear-thinning exponent  $c$  is determined from the fit of  $\mu_f k_{rg}(S_w)$  data to a power function of  $v_g$  or  $N_{cg}$ .

### 4.3 Calibration of $F_2$ function

$F_2$  function has to be calibrated from the normalized texture values determined as above for a fixed value of gas velocity in order to decouple shear-thinning effects from texture variation between the LQR and the HQR. The  $F_2$  function determined for different values of gas velocity is expected to be invariant by construction of the SE model.

$F_2$  transition parameter can be estimated from the slope of  $F_2(S_w)$  function at  $S_w^*$  value, i.e. for a value of  $F_2$  equal to  $\frac{1}{2}$ . Actually,  $F_2$ -function derivative with respect to  $S_w$  is expressed as  $\frac{\Theta}{\pi} \frac{1}{1+[\Theta(S_w-S_w^*)]^2}$  that is  $\frac{\Theta}{\pi}$  for  $S_w = S_w^*$ . In practice, one can determine graphically these two parameters by plotting the normalized texture values  $n_D(S_w)$ . First,  $S_w^*$  is the saturation value for which the function  $n_D$  equals  $\frac{1}{2}$ :

$$S_w^* = n_D^{-1} \left( \frac{1}{2} \right). \quad (25)$$

Once  $S_w^*$  is identified, the parameter  $\Theta$  is determined by evaluating the  $n_D$  function slope at this saturation point:

$$\Theta = \pi \frac{dn_D}{dS_w} (S_w^*). \quad (26)$$

The latter graphical method is accurate if the dimensionless foam texture  $n_D$  data covers the transition range between the LQR and the HQR. Otherwise,  $S_w^*$  and  $\Theta$  can only be roughly estimated and a least-square method may be used to further adjust those parameters.

In summary, our methodology for parameterizing the foam SE model consists in a deterministic processing of apparent foam viscosity data to obtain a discrete set of (experimentally-derived) values of saturation and texture to feed Eq. 18. By comparison with usual methods based on the overall calibration of SE model parameters, the proposed methodology leads to calibrate shear-thinning exponent and texture function sequentially, thanks to the input of a rheological law of foam gas bubbles (or lamellas) into Darcy's flow equations. The method is convenient for the reservoir engineer in charge of the setting-up of a foam SE model for reservoir assessment purposes, because (s)he disposes then of a single model that is consistent with available experimental data. However, the physical accuracy and exactness and that model remain dependent on the quality and amount of experimental foam flow data,

and also of conventional relative permeability data. Actually, the methodology cannot palliate the consequence of scarce or noisy data on the uncertainty of the resulting foam SE model: that relevant issue is not dealt with in our paper.

#### 4.3.1 Determination of $M_{ref}$

As already mentioned for  $F_2$  function,  $M_{ref}$  calculation according to Eq. 17 only requires to input the value of  $c_f n_f^{max}$ , the shear-thinning exponent  $c$  and the reference gas velocity used to defined  $F_4$  function. In practice, that reference velocity is the lowest applied or applicable velocity above velocity threshold for foam generation.

## 5 Application: Scaling of foam parameters with respect to $k$

### 5.1 Foam displacements experimental data

The experiments under consideration [43] consist in foam displacements in three Fontainebleau sandstone cores. Table 1 summarizes the properties of these three cores. The first two cores are homothetic with regard to their pore structure but the third low-permeability core has a slightly different pore structure from the other two as revealed by the  $P_c$  curves shown in Section 5.4.

Table 1: Core samples properties [43].

Core	Diameter (cm)	Length (cm)	$\Phi$ (%)	$k$ (mD)
1	2.4	8.8	12	368
2	2.4	13.1	11.7	121
3	2.4	15.4	10.9	55

The gas phase is composed of 80 % of carbon dioxide and 20 % of methane, and the aqueous phase of synthetic desulfated sea water, wherein a 5 g/L surfactant is dissolved to generate foam. The thermodynamic conditions are 60 °C and 80 bar. For each of the three cores, a set of displacements was performed with different values of the foam quality. Each experiment at a given quality begins with the co-injection of brine and gas at different total flow rates respecting the selected quality value. The pressure drop is recorded at steady state at each selected total flow rate. The same injection sequence at a given quality and different total flow rates is then performed again, but with the surfactant solution instead of brine in order to generate foam. After the highest flow rate has been applied, foam is re-injected at the initial rate to measure the hysteresis of foam mobility. However, these hysteresis effects are not investigated herein. For all displacements, the pressure drop was continuously recorded until steady-state flow was reached. Raw pressure drop data were averaged to smooth unavoidable fluctuations in the presence of foam. The apparent foam viscosity is then determined as  $\mu_f = \frac{k}{u} \frac{\Delta P}{L}$ , where  $\Delta P$  is the pressure drop at steady state and  $L$  the core length. Finally,  $\mu_f$  is determined as a function of foam quality  $f_g$  and total velocity  $u$ , which constitutes the main result of foam displacement experiments on a given core.

## 5.2 Calibration of foam flow models

Experimental foam flow results are used to calibrate a SE foam flow model for each of the three cores, 1, 2 and 3. Core 3 data are however less reliable than the ones acquired on cores 1 and 2. Two modelling procedures are used. First, we apply one of the numerous published methods that consist in a least-square minimization of the differences between experimental apparent viscosity data and the ones predicted by the SE model. Then, we apply our method based on the identification of SE foam model to a PB model.

Regarding published methods, we adopted the least-square minimization implementation method proposed by Farajzadeh et al [21], because both pressure drop and water saturation data are incorporated in the objective function instead of pressure drop data alone, in order to better constrain model calibration. The set of foam model parameters,  $Y = (M_{\text{ref}}, S_w^*, \Theta, e_c)$ , was adjusted using a least-square method applied over a discrete domain of values limited by two lower and upper bounds chosen respectively equal to  $(10^2, S_{wr}, 10, 0.1)$  and  $(10^4, S_{wr} + 0.3, 10^4, 0.8)$ . The SE foam model parameters calibrated with that method are given in Table 3.

Regarding our modelling methodology, we start with the determination of the shear-thinning exponent. For this purpose, the products  $\mu_f k_{rg}(S_w)$  at different total flow velocities and given quality are adjusted to a power law function with the shear-thinning exponent as adjustable parameter, according to previous developments (see Section 4). As shown in Fig. 4, adjusted  $c$  values for the different foam qualities are very close and an average  $c$  value can be retained for any given core. This average  $c$  value does not much vary from one core to another, as reported in Table 3; as a consequence we did not attempt to identify any scaling law later in this paper.

Then, we proceed with the calibration of the dry-out function  $F_2$ . To that end, the  $c_f n_f$  values calculated using Eq. 19 are plotted against foam quality, in order to determine the maximum  $c_f n_f$  product, that is equal to  $c_f n_f^{\text{max}}$  since  $c_f$  is invariant for a given foam-rock system. The maximum foam texture  $n_f^{\text{max}}$  is estimated from the characteristic pore size of the core under consideration (estimated itself from its porosity and permeability as specified before). Results are shown in Fig. 5.

The dimensionless texture  $n_D$  can then be calculated and drawn versus saturation according to Eq. 19 and Eq. 20 for each flow experiment characterized by given values of foam quality and total velocity. The so-determined  $n_D(S_w)$  function can then be used to calibrate the constants  $S_w^*$  and  $\Theta$  of the dry-out function  $F_2$ . A least-square method of adjustment was used and applied to the sole experimental data at low velocity that best reflect the texture effects and are also less dispersed (see Fig. 6). Indeed, the SE foam model implicitly assumes that  $F_2$ , and in particular  $S_w^*$ , is independent of flow rate whose effect is accounted for by function  $F_4$ . Invariant  $S_w^*$  is also consistent with the concept of fixed limiting capillary pressure  $P_c^*$  as explained by Zhou and Rossen [44]. To end with the SE-PB models identification, the optimal gas mobility reduction  $M_{\text{ref}}$  is calculated from Eq. 18. To summarize, the above calibration sequence turns out to be an almost-fully deterministic treatment procedure of experimental data based on a transcription of apparent viscosity measurements in terms of both saturation and texture. Of course, the resulting foam model remains an approximate model, which is inherent to the usual noise observed on foam flow data and to the underlying assumptions of the foam flow model, such as the absence of any capillary effects.

The steady-state PB model parameters obtained from the identification method are given in Table 2 and the calibrated SE foam model parameters using the two methods are reported in Table 3.

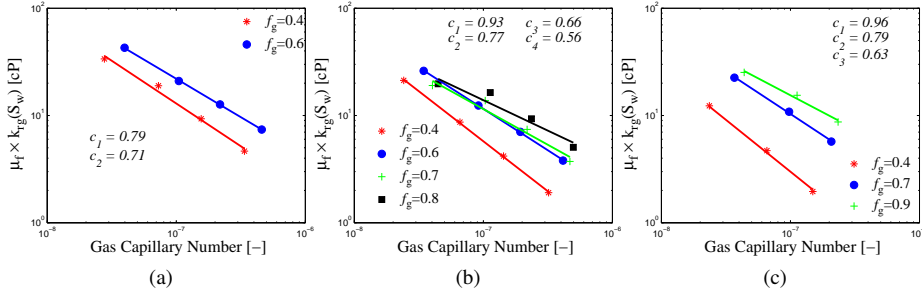


Fig. 4: Adjustment of flow rate-scan experiments at low-quality regime by power laws in order to determine the shear-thinning exponent: (a) core 1, (b) core 2 and (c) core 3. The lines represent adjusted power law functions and the symbols the experimental data.  $c_i$  values correspond to the adjusted exponents for each foam quality. The shear-thinning exponent  $c$  for a given core is taken equal to the average of the  $c_i$  values.

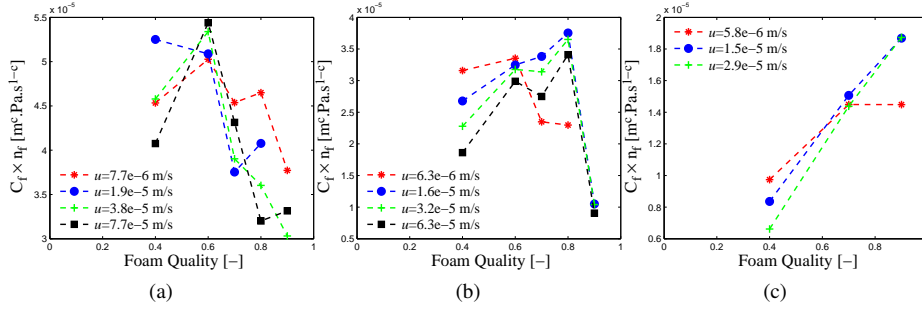


Fig. 5: Variation of the product  $c_f n_f$  versus foam quality: (a) core 1, (b) core 2 and (c) core 3 (dashed lines represent visual guides for the variation at constant total velocity and symbols the measurements).

Table 2: Adjusted steady-state PB model parameters with respect to apparent foam viscosity measurements. The constant  $c$  shown in the unit of  $c_f$  is the calibrated shear-thinning exponent for each core.

Core	$c_f$ (m <sup>1+c</sup> · Pa · s <sup>1-c</sup> )	$n_L^{\max}$ (m <sup>-1</sup> )
1	$3.56 \times 10^{-10}$	$1.52 \times 10^5$
2	$1.42 \times 10^{-10}$	$2.63 \times 10^5$
3	$0.50 \times 10^{-10}$	$3.75 \times 10^5$

To test the predictive capacity of the SE model calibrated before, the foamed-gas fractional flow and the apparent foam viscosity calculated with that model were compared with the experimental data. To that end, we first solve analytically the fractional flow equation

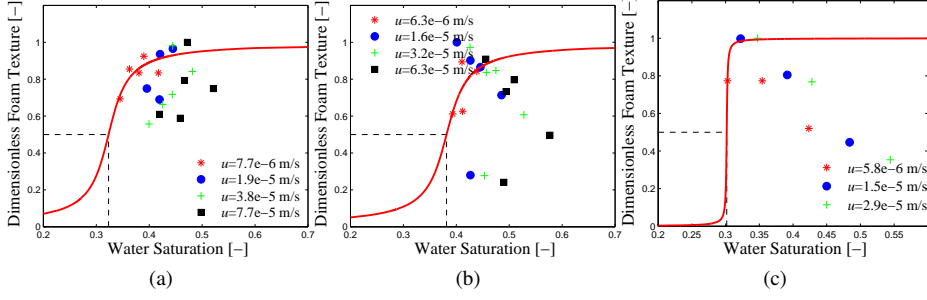


Fig. 6: Variation of dimensionless foam texture versus water saturation as inferred from the identification method: (a) core 1, (b) core 2 and (c) core 3. The continuous lines represent the adjusted  $F_2$  function with respect to the lowest velocity and the points are the experimental data.

Table 3: Adjusted foam model parameters with respect to experimental data obtained from both Farajzadeh et al [21] method and our modelling methodology based on SE-PB identification.

Core	$M_{\text{ref}}$	$S_w^*$	$\Theta$	$N_{cg}^{\text{ref}}$	$c = e_c$
Farajzadeh et al method					
1	4342	0.34	424	$2.77 \times 10^{-8}$	0.72
2	2983	0.39	308	$2.77 \times 10^{-8}$	0.76
3	2055	0.28	549	$2.77 \times 10^{-8}$	0.67
SE-PB identification					
1	5317	0.32	36	$2.77 \times 10^{-8}$	0.75
2	3002	0.38	34	$2.77 \times 10^{-8}$	0.73
3	2736	0.30	$10^3$	$2.77 \times 10^{-8}$	0.79

obtained by expressing the foam mobility in Eq. 7 with the SE-model formulation, that is:

$$f_g(Y; S_g) = \frac{1}{1 + \frac{\mu_g}{\mu_w} \frac{k_{rw}(S_g)}{FM(Y; f_g, S_g) k_{rg}(S_g)}}, \quad (27)$$

where  $Y$  is one of the two sets of SE-model parameters given in Table 3. In practice, the foamed-gas fractional flow versus gas saturation was constructed by finely discretizing the variation interval  $]0, 1[$  of  $f_g$  and calculating for each point the corresponding gas saturation  $S_g$  by inverting Eq. 27. Then, we used the  $f_g$ - $S_g$  relationship in order to compute the SE-model apparent viscosity from  $\frac{1}{\mu_f} = \frac{k_{rw}}{\mu_w} + \frac{FM k_{rg}}{\mu_g}$ . Comparison results are shown in Fig. 7. The comparison is shown for both models calibrated with either the least-square method or the SE-PB identification method. We found that the foamed-gas fractional flow, the maximum apparent foam viscosities and the transition between low- and high-quality regimes are fairly-well matched for the two first cores using either our method or Farajzadeh et al method. We note that the  $\Theta$  values, as obtained by either method and equal to respectively about 35 and 360 (see Table 3), do not much change the saturation transition. Indeed, high  $\Theta$  values, such as the ones found by either method, yield a stiff saturation front.

The relative error on foam apparent viscosities between our calibrated model and experiments was calculated for each core, excluding the less reliable values for  $f_g = 0.9$  (in the coalescence regime). The average error was found equal to 10% for cores 1 and 2 and 16% for core 3. Actually, experimental data are less reliable for core 3 even in the low-quality regime. This issue is clear on Fig. 6(c) since it shows that the foam texture decreases with water saturation in the low-quality regime, which is unexpected, and consequently cannot be captured by the  $F_2$  function of an SE foam model that assumes a constant foam texture in the low-quality regime. Due to the poor consistency of core 3 data, some reserves will be taken in the scaling of foam model parameters with respect to the permeability, as discussed in the following section of that paper.

### 5.3 Theoretical approaches for scaling with respect to permeability

In this section, scaling trends of foam parameters with respect to permeability are searched for. To that end, the results from previous section (Table 3) are analyzed according to two viewpoints, namely a quasi-static viewpoint and a dynamic viewpoint which are described below. The SE-PB results obtained with the SE-PB identification method are considered for that analysis.

#### 5.3.1 Quasi-static viewpoint

To begin with, a quasi-static viewpoint of foam flow at low velocities is considered. That is, capillary pressure is assumed to determine film stability within the porous medium during foam flow. Under this assumption, foam coalescence, i.e. the transition between LQR and HQR, occurs when the gas-water capillary pressure reaches a maximum value that is close to the disjoining pressure of the foam under consideration [45]. That disjoining pressure is a characteristic of the foam and is independent of the porous medium, whereas the saturation corresponding to that pressure is a function of the properties of the porous medium under consideration and inferred from its capillary pressure curve. This leads us to assume that foam coalescence starts when the saturation corresponds to a fixed critical value of the capillary pressure, that is equal to the characteristic disjoining pressure of the foam under consideration, whatever the porous medium properties.

#### 5.3.2 Dynamic viewpoint

That viewpoint considers the conditions of rupture of films flowing in pores. Film rupture occurs dynamically through a shear process when the transverse gradient of film local velocity within pore (film shear), denoted  $dw/dy$  (derivative of the local velocity within a pore with respect to distance  $y$  from pore axis), exceeds a given threshold value  $w'_{\max}$  that is a characteristic of the foam under consideration. For a laminar (Poiseuille) flow of gas in a capillary tube of radius  $r$ ,  $dw/dy$  is maximum at pore wall and equal to  $\frac{r}{2\mu}|\nabla P|$ . Therefore, the limit of stability of films is reached for a pressure gradient  $|\nabla P|_{\max}$  equal to  $2\mu w'_{\max}/r$ , i.e. inversely proportional to characteristic pore radius  $r$ . To that maximum pressure gradient corresponds a maximum value of the dynamic capillary pressure within the porous medium, called the critical capillary pressure  $P_c^*$ . Therefore,  $P_c^*$  is also inversely proportional to  $r$  or  $\sqrt{k}$ .

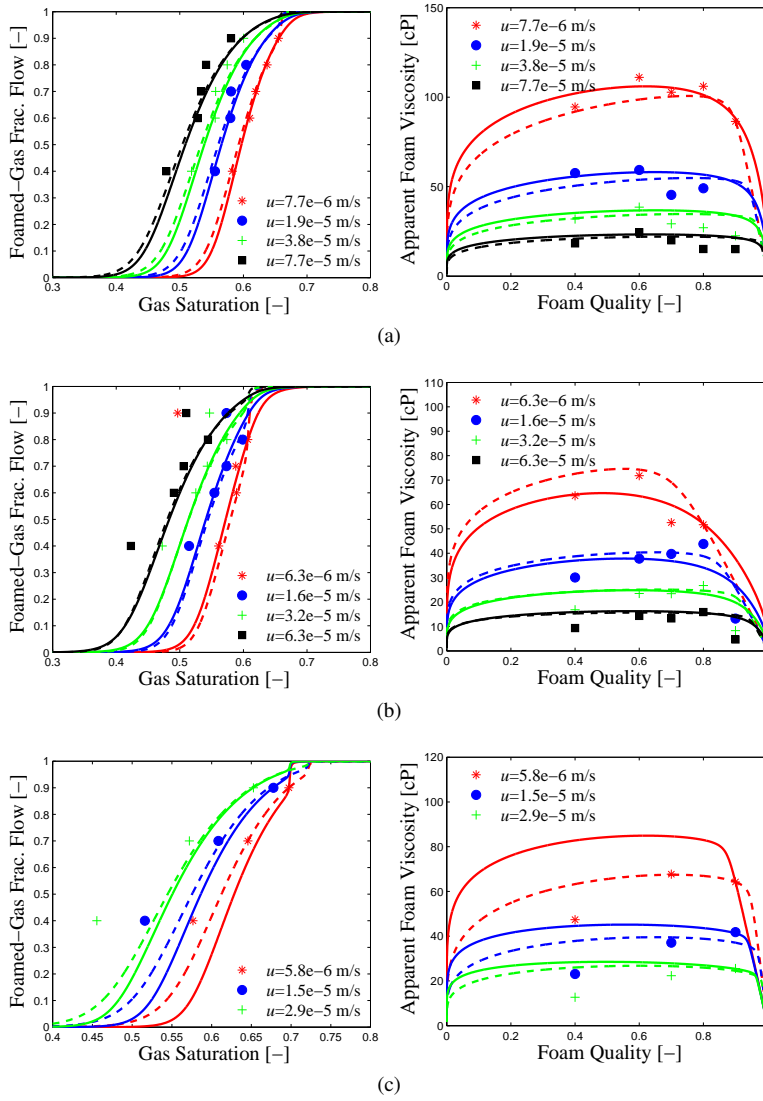


Fig. 7: Comparison between the computed foamed-gas fractional flow and apparent foam viscosity, and the corresponding experimental data: (a) core 1, (b) core 2 and (c) core 3. The lines represent the computed results (dashed lines for Farajzadeh et al method and solid lines for the SE-PB identification method) and the symbols the experimental data.

#### 5.4 Scaling of $P_c^*$ and $S_w^*$

Let us examine the evolution of  $S_w^*$  and  $P_c^*$  for the three cores. Regarding  $S_w^*$ , Table 3 shows an increase of  $S_w^*$  when the permeability decreases for cores 1 and 2 that have the same pore structure (i.e. homothetic, following the same Leverett J-function). That result is con-

sistent with the observations from other authors, Farajzadeh et al [21], Khatib et al [20]) and Kapetas et al [46].

Regarding the critical capillary pressure,  $P_c^*$  values were simply determined from the  $P_c$  curves of Fig. 8(a) for the calibrated  $S_w^*$  values of Table 3. The resulting  $P_c^*$  values for the 3 cores are shown in Fig. 8(b) as a function of permeability.  $P_c^*$  values that are respectively equal to 80, 110 and 170 mbar for cores 1, 2 and 3, are found to decrease with increasing permeability, with an evolution trend close to  $1/\sqrt{k}$  as reported in published studies from Khatib et al [20] and Farajzadeh et al [21].

Interpretation of such results is discussed as follows. To begin with, the *quasi-static viewpoint* of foam flow at low velocities is considered. Retaining a fixed- $P_c^*$  assumption for given foam, the inversion of  $P_c$  function for  $P_c^*$  leads to a  $S_w^*$  value that necessarily increases for homothetic porous media of decreasing permeability (like cores 1 and 2). The reason is that (a) gas-water  $P_c$  is a monotonous decreasing function of  $S_w$ , and (b)  $P_c$  increases when the permeability of homothetic cores decreases. We tried to verify if previous interpretation was consistent with the  $S_w^*$  values calibrated for homothetic cores 1 and 2. To that end, we determined  $P_c^*$  as the  $P_c$  value of core 1 at the critical saturation (given in Table 3) then inverted the  $P_c$  function of core 2 for that fixed  $P_c^*$  value. Unfortunately, the  $S_w^*$  determined this way for core 2 was about 0.83 which is much higher than the actually-calibrated value of Table 3. Finally, it turns out that a fixed- $P_c^*$  assumption appears to be qualitatively consistent with the increase of  $S_w^*$  with decreasing permeability, but is not valid at all from a quantitative standpoint. In addition, the actual evolution of  $P_c^*$  with  $k$  is in contradiction with the quasi-static viewpoint that predicts a transition between LQR and HQR at a fixed  $P_c^*$  value.

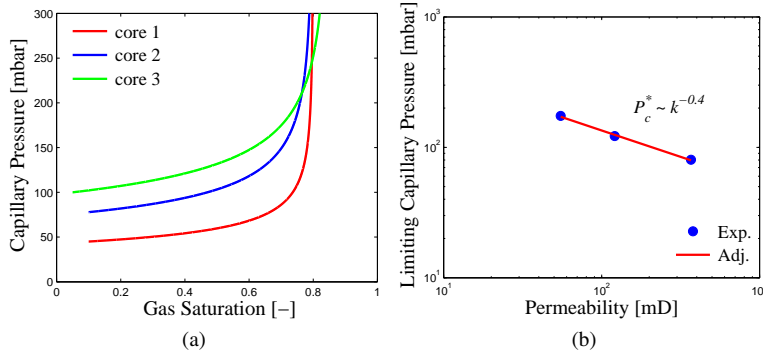


Fig. 8: (a) Gas water capillary pressure curves used for each core; (b) Effect of permeability on the limiting capillary pressure  $P_c^*$ . The points are estimated from the water saturation  $S_w^*$  given in Table 3 using the SE-PB identification method and the line is a power law adjustment. The optimal adjustment yields  $P_c^* \sim k^{-0.4}$  for the 3 cores.

Interpretation was then attempted from a *dynamic standpoint*. Actually, the dynamic viewpoint of film stability is fully consistent with the observed evolution of  $P_c^*$  with the permeability. However, such a scaling of  $P_c^*$  as  $1/\sqrt{k}$  implies that  $S_w^*$  remains constant for homothetic porous media, whereas an increase of  $S_w^*$  with decreasing permeability, although moderate, is observed.

In order to further specify the evolution of  $S_w^*$  with  $k$ , we first adjust the  $P_c^*$  curves of our cores to capillary pressure power functions as proposed by Brooks and Corey [47], i.e.

$P_c(S) = \frac{P_e}{S^{1/\lambda}}$ , where  $P_e$  is the entry capillary pressure,  $S$  the normalized water saturation and  $\lambda$  the pore size distribution index. A value of  $\lambda$  equal to 3 provides a good fit of our  $P_c$  curves. Then a relation between  $S_w^*$  and  $P_c^*$  can be formulated by inverting the  $P_c$  function for  $P_c^*$ , leading to  $S_w^* = S_{wr} + (1 - S_{wr} - S_{gc})(P_e/P_c^*)^\lambda$ . Inserting the scaling law of  $P_c^*$  in the latter expression of  $S_w^*$  and knowing that  $P_e \sim 1/\sqrt{k}$  for homothetic media yields  $S_w^* \sim k^{\lambda(\alpha - \frac{1}{2})}$ . For  $0 < \alpha < \frac{1}{2}$ , both the critical water saturation and the critical capillary pressure increase with decreasing permeability. In our case,  $S_w^* \sim k^{-0.3}$  for the two homothetic cores.

To end with, neither the quasi-static interpretation model (fixed  $P_c^*$ ), nor the dynamic one (fixed  $S_w^*$ ), explain both  $S_w^*$  and  $P_c^*$  evolutions with  $k$ . The reality seems to lie between these two models but looks closer to the dynamic one, such that  $P_c^* \sim 1/k^\alpha$  with  $\alpha \leq \frac{1}{2}$ .

### 5.5 Scaling of $\Theta$

Regarding the transition parameter  $\Theta$ , results from Table 3 do not clearly indicate a trend in the evolution of  $\Theta$  with permeability. Considering the first two homothetic cores,  $\Theta$  seems more or less invariant. Including the third non-homothetic core in the analysis (although this is not rigorous on a physical standpoint),  $\Theta$  seems to increase with decreasing permeability. Such evolution is in agreement with Farajzadeh et al findings [21].

We will nevertheless try to establish what is the expected evolution of  $\Theta$  with  $k$  based on the analysis of the  $F_2$  function where  $\Theta$  is the driving parameter:

$$F_2(S_w) = \frac{1}{2} + \frac{1}{\pi} \arctan[\Theta(S_w - S_w^*)].$$

The  $F_2$  function quantifies the increase of gas phase mobility due to foam coarsening when the gas saturation increases beyond a certain limit denoted  $1 - S_w^{\text{opt}}$ .  $S_w^{\text{opt}}$  is the optimal water saturation below which foam coalescence occurs ( $F_2 \approx 1$  for  $S_w \geq S_w^{\text{opt}}$ ). A symmetrical arctan function of  $S_w$  centered on the critical saturation  $S_w^*$  is adopted for modelling that coalescence. This implies that foam vanishes completely ( $F_2 \approx 0$ ) and original gas mobility is restored when  $S_w$  equals  $S_w^{\text{min}}$  such that  $S_w^{\text{opt}} - S_w^* = S_w^* - S_w^{\text{min}}$ .  $\Theta$  drives the decrease of  $F_2$  with  $S_w$ . Actually, the derivative of  $F_2$  with respect to  $S_w$  is equal to:

$$\frac{dF_2}{dS_w} = \frac{\Theta}{\pi} \frac{1}{1 + [\Theta(S_w - S_w^*)]^2}.$$

By linearizing that symmetrical  $F_2$  function in the vicinity of  $S_w^*$  where  $\frac{dF_2}{dS_w}$  equals  $\frac{\Theta}{\pi}$ , the width of the saturation transition, i.e.  $S_w^{\text{opt}} - S_w^{\text{min}}$ , can be approximated as:

$$S_w^{\text{opt}} - S_w^{\text{min}} = \frac{F_2(S_w^{\text{opt}}) - F_2(S_w^{\text{min}})}{\left(\frac{dF_2}{dS_w}\right)_{S_w^*}} = \frac{1}{\left(\frac{dF_2}{dS_w}\right)_{S_w^*}} = \frac{\pi}{\Theta}. \quad (28)$$

The question raised is that of determining the evolution of  $\Theta$  with the permeability. Again, we have to consider either of the two quasi-static and dynamic viewpoints of foam flow within porous media. Scaling relationships according to these two viewpoints are established in Appendix B.

In summary, from the static viewpoint, the evolution of  $\Theta$  as a function of  $k$  is given by:

$$\Theta = \Theta_{\text{ref}} \frac{\left(\frac{dS_w}{dP_{e,\text{ref}}}\right) \Pi}{\left(\frac{dS_w}{dP_c}\right) \Pi}. \quad (29)$$

That evolution of  $\Theta$  cannot be predicted a priori from this relationship, even for homothetic porous media, because it depends on the shape of the  $P_c$  curve with respect to the value of  $\Pi$ . We did not test this relationship against our calibrated  $\Theta$  values because the assumption of fixed  $P_c^*$  is not verified.

From the dynamic viewpoint, the following general relation between  $\Theta$  and  $\Theta_{\text{ref}}$  holds for any couple of porous media (even non homothetic media):

$$\Theta = \Theta_{\text{ref}} \frac{r \left( \frac{dP_c}{dS_w} \right)_{S_w^*}}{r_{\text{ref}} \left( \frac{dP_{c,\text{ref}}}{dS_w} \right)_{(S_w^*)_{\text{ref}}}}. \quad (30)$$

This relationship implies that the transition parameter  $\Theta$  is invariant for homothetic porous media.

The SE-PB identification (Table 3) shows that  $\Theta$  values for homothetic cores 1 and 2, i.e. 36 and 34, are quasi-identical, which is in line with the dynamic assumption of foam coalescence.

Regarding core 3 that is not homothetic with the other two cores, one can check if the general scaling relationship (Eq. 30) established under dynamic assumption makes possible the estimation of  $\Theta$  for core 3 from the value determined for core 1 for instance. We assume that the characteristic radii for cores 1 and 3 scale as  $\sqrt{8k/\Phi}$  although this may not be legitimate for non-homothetic cores (underlying assumption is that for these samples of the same sandstone, essentially the shape of the  $P_c$  curves is modified). Then,  $r_3/r_1$  is equal to 0.4 from the  $(k, \Phi)$  data of Table 1, and the ratio of the  $P_c$  derivatives at core critical saturation between core 3 and core 1 is close to 1.7, from Fig. 8(a) with  $S_w^*$  values of Table 3 for SE-PB identification method. Hence, the transition parameter for core 3 should not differ much from that for core 1: such a calculation would predict a  $\Theta_3$  value of 25. That prediction is not in line with the actually-calibrated value, which is of the order of 1000. In reality, we have to keep in mind that the sensitivity of the transition parameter is very high for foams. Hence, its calibration is uncertain and very approximate if we also consider the high dispersion of raw experimental data.

## 5.6 Scaling of $M_{\text{ref}}$

For a given foam, the mobility reduction  $M_{\text{ref}}$  represents the ratio between the continuous gas mobility  $k_{rg}/\mu_g$  and the foamed-gas mobility that is defined as  $k_{rg}^{\text{SE}}/\mu_g$  in SE models, or as  $k_{rg}/\mu_g^{\text{PB}}$  in PB models, at optimal foaming conditions. Scaling  $M_{\text{ref}}$  for different porous media characterized by the same  $k_{rg}$  functions can then be reduced to the scaling of  $\mu_g^{\text{PB}}$ . Analogy between flow in a capillary tube (originally formulated by Bretherton [32]) and flow in a porous medium has led most authors to use the empirical rheological law given by Eq. 5 for foamed-gas. Eq. 17 for  $M_{\text{ref}}$  tells us that, for a given velocity, the mobility reduction is at the first order determined by the product of constant  $c_f$  and maximum texture  $n_f^{\text{max}}$ .

Kovscek and Bertin [23] derived an expression of  $\mu_g^{\text{PB}}$  scaled with respect to rock permeability and capillary pressure by establishing an equivalence between rheological law given by Eq. 5 and Hirasaki and Lawson's formula [12] for the apparent viscosity of a train of bubbles of pre-determined volume flowing in a capillary tube, that is:

$$\mu_g^{\text{PB}} = 0.85 \mu_w \frac{n_L}{r_c} (r^2 + r_c^2) \left( \frac{\sigma}{3\mu_w v_g} \right)^{\frac{1}{3}}, \quad (31)$$

where  $r$  is the tube radius and  $r_c$  the curvature radius of the Plateau borders separating gas bubbles. That formula assumes that touching bubbles are flowing through the capillary and that the surface tension gradient effects on effective gas viscosity are negligible. Actually, that expression of the effective viscosity can be considered for scaling purpose, because it is related to the geometrical characteristics of capillary tubes, or to the properties of the equivalent porous medium represented as a bundle of such capillary tubes. In the following, we consider again the formula given by Eq. 31 for apparent foam viscosity; however, our analysis differs from the development made by Kovscek and Bertin.

For a given foam flowing in a porous medium of permeability  $k$  and porosity  $\Phi$ , capillary tube radius  $r$  is equivalent to the quantity  $\sqrt{8k/\Phi}$  and  $r_c$  is related to the disjoining pressure of the films of the foam under consideration [45].  $r_c$  is therefore assumed invariant for the same foam displaced through different porous media. Furthermore, we assume that  $r_c$  is negligible compared to pore radii (such an assumption may not be valid however in very-low-permeability media). Therefore,  $\mu_g^{\text{PB}}$  scales as  $n_L r^2$  under given velocity conditions. For homothetic porous media of different permeabilities with similar porosities,  $r$  scales as  $\sqrt{k}$  and the lineic foam texture,  $n_L$ , that is proportional to  $1/r$  (see Section 4), scales as  $1/\sqrt{k}$ , hence  $\mu_g^{\text{PB}}$  scales as  $\sqrt{k}$ . To end with, above analysis indicates that  $M_{\text{ref}}$  is expected to increase as the square root of permeability for homothetic porous media of different permeabilities. That scaling approximation neglects small porosity variations compared to permeability variations in many natural porous media.

Analysis of  $M_{\text{ref}}$  results for homothetic samples 1 and 2 is consistent with the previous relationship. Indeed, for homothetic cores 1 and 2, Table 3 indicates that, according to our modelling methodology by SE-PB models identification,  $M_{\text{ref},2} = 3002$  is very close to the scaled value derived from core 1, that is  $M_{\text{ref},1} \sqrt{k_2/k_1} = 5317 \sqrt{121/368} = 3049$ . The low-permeability core 3 is characterized by a pore structure slightly different from that of cores 1 and 2. Its  $M_{\text{ref}}$  value is also lower than the values for cores 1 and 2 but scaling permeability exponent differs from  $\frac{1}{2}$ . The dependence of the parameter  $M_{\text{ref}}$  on the permeability  $k$ , as obtained from Table 3, is shown in Fig. 9.

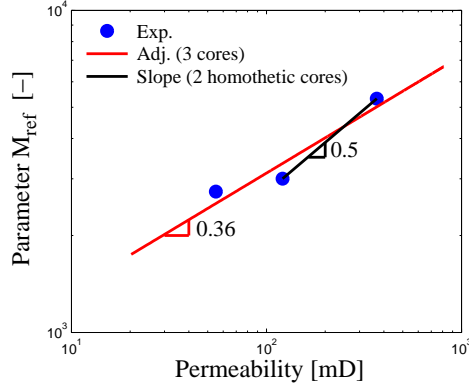


Fig. 9: Dependence of  $M_{\text{ref}}$  to the permeability  $k$ . Note that the adjustment includes three cores although the third core has a slightly different pore structure. The optimal adjustment yields  $M_{\text{ref}} \sim k^{0.36}$ . The data of the homothetic cores 1 and 2 show that  $M_{\text{ref}} \sim \sqrt{k}$ .

To conclude, the evolution of foam mobility reduction  $M_{\text{ref}}$  with porous medium permeability is found to follow the scaling laws derived from an equivalence between foam flow in a porous medium and foam flow in capillary tubes. Such results are worth being investigated further on the basis of more extensive data set acquired on well-characterized porous media.

### 5.7 Summary of foam parameters scaling trends with respect to $k$

Table 4 summarizes the scaling of SE model parameters with permeability according to the two theoretical models for films stability considered before. The dynamic viewpoint seems to account for the transition between the LQR and the HQR better than the static viewpoint. However, interpretation may be more complex because foam texture is continuously changing under critical conditions and because gas trapping and hysteresis phenomena might be involved [48,49]. By taking into account the capillary properties of the porous medium in the modelling, foam flow properties under the so-called critical conditions might be better explained and predicted. To that end, well-documented experimental data that cover the whole transition in foam flow regime should also be acquired.

Table 4: Scaling trends summary for homothetic porous media.

<i>Theoretical model for films stability</i>	STATIC PICTURE	DYNAMIC PICTURE	OBSERVATION
<i>Expected evolution of <math>P_c^*</math> with <math>k</math></i>	Constant $P_c^*$	$P_c^* \sim 1/\sqrt{k}$	$P_c^* \sim 1/k^\alpha$ with $\alpha \leq \frac{1}{2}$
<i>Expected evolution of <math>S_w^*</math> with <math>k</math></i>	$S_w^*$ increase with $k$ decrease	Constant $S_w^*$	Moderate $S_w^*$ increase with $k$ decrease as $S_w^* \sim k^{\lambda(\alpha - \frac{1}{2})}$
<i>Expected evolution of <math>\Theta</math> with <math>k</math></i>	$P_c$ -dependent	Constant $\Theta$	Quasi-constant
<i>Expected evolution of <math>M_{\text{ref}}</math> with <math>k</math></i>	$M_{\text{ref}} \sim \sqrt{k}$		

Among the scaling relationships established in previous subsections, the scaling of foam performance ( $M_{\text{ref}}$ ) with permeability is of particular importance for reservoir engineering purposes because foam processes are primarily dedicated to reservoirs where the detrimental impact of heterogeneities on displacement has to be alleviated. In the following subsection, numerical simulations highlight the significance of that scaling with respect to permeability.

### 5.8 Significance of foam model scaling with respect to $k$

Two scaled SE foam models following the scaling laws determined from the previous analysis of core data are used to simulate foam flow displacement in a simple reservoir cross-section made up of two layers of equal thickness (10 m) and different porosity and permeability, respectively 10 % and 100 mD for upper layer 1, 18 % and 1600 mD for lower layer 2. Both layers are initially saturated with additive-free water. A foam of quality 0.6 is injected at a flow rate of 26.4 m<sup>3</sup>/day. Initial pressure, of 100 bar, is kept constant at production well while injection pressure is allowed to rise during foam displacement. The experimentally-derived scaling laws established before for  $M_{\text{ref}}$  and  $S_w^*$ , respectively as  $\sqrt{k}$  and  $k^{-0.3}$  are applied. To test the significance of these scaling laws, the same simulation is

performed again without any scaling, i.e. by using the foam flow model parameters of layer 1 in both layers. Scaling laws according to theoretical dynamic interpretation of permeability effects, i.e.  $M_{\text{ref}}$  evolution as  $\sqrt{k}$  and constant  $S_w^*$ , were also considered. Very close results were obtained in both cases. Simulated results with and without  $k$ -scaling are illustrated by Figure 10(a) for the produced gas fractional rate as a function of injected pore volumes, and by Fig. 10(b) for the in situ water saturation distribution as a function of injected pore volumes. Differences are significant although the permeability contrast under consideration is reasonable if one refers to reservoirs with contrasted facies properties or to fractured formations.

## 6 Conclusion and perspectives

A new methodology based on an equivalence with a foam texture model has been implemented to calibrate the steady-state implicit-texture model to predict foam flow effects on gas mobility in reservoir simulators. This calibration involves a deterministic processing of steady-state foam flow data measured with different foam qualities and velocities. The method was applied to foam flow data set measured on three sandstones of different permeabilities, both for demonstrating the advantage in terms of model robustness, and for elucidating the scaling of foam flow model parameters with respect to porous medium properties. The following main conclusions can be drawn:

- (a) A steady-state semi-empirical foam model can be calibrated thanks to a deterministic processing of experimental steady-state apparent viscosity data, including the transition between the two low-quality and high-quality regimes. Calibration may however remain approximate for incomplete or scattered data sets such as the one acquired on the low-permeability core under consideration in this study.
- (b) Scaling trends of foam parameters with porous medium permeability were found consistent with other published observations and interpreted:
  - The shear-thinning function that models the flow velocity impact on foam mobility appears to be fairly invariant for cores of different permeabilities, with a characteristic exponent close to 0.7.
  - For homothetic porous media, the critical water saturation  $S_w^*$  increases slightly when the permeability decreases; accordingly, the critical capillary pressure  $P_c^*$  increases according to a law close to  $1/\sqrt{k}$  but maybe not exactly if one considers the  $S_w^*$  change. Interpretation of such results was attempted thanks to two static and dynamic viewpoints of foam bubbles coalescence within porous media. The dynamic viewpoint seems to be more relevant than the (quasi-)static viewpoint because the latter implies a fixed  $P_c^*$  whatever the porous medium, which is not verified experimentally.
  - The evolution of transition parameter between low-quality and high quality regimes for different porous media has been formulated according to the static and dynamic viewpoints of foam coalescence. The quasi-invariance of calibrated  $\Theta$  values for the two homothetic cores is consistent with the dynamic viewpoint.
  - The main scaling trend is an increase of the mobility reduction ratio  $M_{\text{ref}}$  as the square root of permeability. This scaling law was inferred from an analogy between foam flow in porous media and foam flow in capillary tubes, and was found consistent with the modelling of available experimental data on three cores, and with other experimental findings.

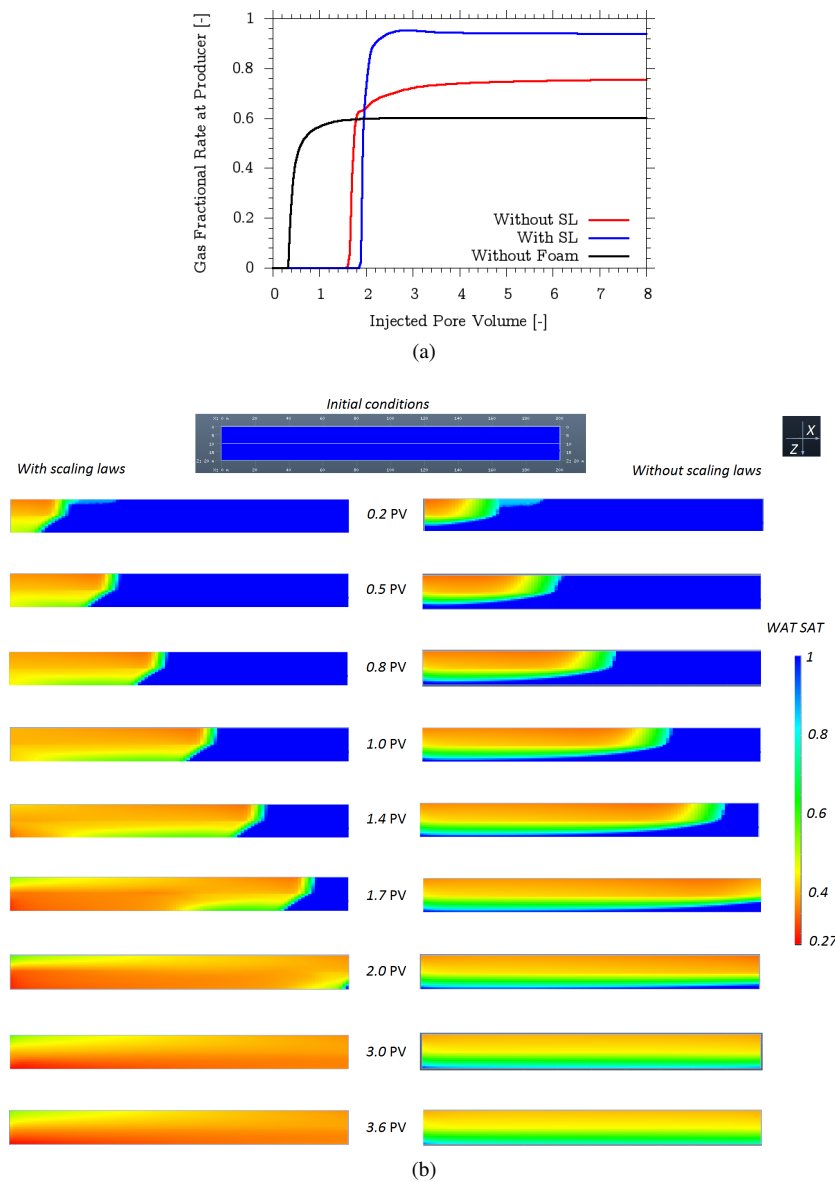


Fig. 10: Comparison of (a) produced gas fractional rate and (b) in situ water saturation as a function of injected pore volumes, with and without rescaling  $M_{ref}$  and  $S_w^*$  in the permeability with experimentally-derived scaling laws (see the text).

(c) The scaling of foam flow model parameters with permeability is shown to significantly impact the predictions of foam flow displacement in a two-layer reservoir with a permeability contrast. Hence, such a scaling, especially of the mobility reduction ratio, is highly recommended for foam process evaluation.

To conclude, we dispose of a robust procedure to analyze and model foam flow measurements in porous media. The scaling trends derived from the analysis of available data require to be further confirmed and extended to natural porous media of different structures and properties, with the help of other extensively-documented and accurate experimental data sets. Indeed, the lack of experimental data does not allow us to draw a definitive conclusion regarding the validity of the dynamic viewpoint of foam coalescence and of the corresponding scaling relationships established in that paper. Notwithstanding, the methodology and physical relationships developed herein should be helpful for the assessment and selection of a foam-based process for improved oil recovery purposes.

### Acknowledgements

The authors thank L. Nabzar and L. G. Pedroni for useful discussions and IFPEN for permission to publish this work.

### A Determination of saturation at steady-state in the presence of foam

The water saturation is determined by taking into account the invariance of relative permeability to water whether foam is present or not. At steady state, the measured pressure drop during foam flow can be written using Darcy's law applied to foam considered as a single fluid or using generalized Darcy's law applied to water phase, that is:

$$\Delta P = \frac{\mu_f u L}{k} = \frac{\mu_w (1 - f_g) u L}{k k_{rw}},$$

Hence, one infers:

$$k_{rw} = \frac{\mu_w (1 - f_g)}{\mu_f}.$$

Power law functions are considered to model relative permeability functions versus saturation in the framework of this paper, that is  $k_{rw} = k_{rw}^0 S^{n_w}$  with  $S = (S_w - S_{wr}) / (1 - S_{wr} - S_{gc})$  the normalized water saturation,  $S_{wr}$  the residual water saturation and  $S_{gc}$  the critical gas saturation.  $k_{rw}^0$  is the maximum relative permeability to water and  $n_w$  the relative permeability exponent. Water saturation can then be determined as:

$$S_w = S_{wr} + (1 - S_{wr} - S_{gc}) \left( \frac{\mu_w (1 - f_g)}{\mu_f k_{rw}^0} \right)^{1/n_w},$$

or more directly from measured steady-state pressure drop as:

$$S_w = S_{wr} + (1 - S_{wr} - S_{gc}) \left( \frac{\mu_w (1 - f_g) u L}{k_{rw}^0 k \Delta P} \right)^{1/n_w}.$$

### B Evolution of transition parameter $\Theta$ with $k$ according to static and dynamic viewpoints

The evolution of transition parameter  $\Theta$  with permeability is discussed, considering either of the two (quasi-) static and dynamic viewpoints of foam flow within porous media.

First, the *static assumption* implies that coalescence of foam occurs over a  $P_c$  interval centered around the  $P_c^*$  value corresponding to the disjoining pressure  $\Pi$  of the foam. That  $P_c$  interval, denoted  $[\Pi^-, \Pi^+]$ , is the same whatever the permeability of the porous medium. For a porous medium of permeability  $k_{ref}$ , the width of the saturation transition, i.e.  $(S_w^{opt})_{ref} - (S_w^{min})_{ref}$ , can then be expressed as  $P_{c,ref}^{-1}(\Pi^-) - P_{c,ref}^{-1}(\Pi^+)$  that is also equal to  $\pi / \Theta_{ref}$ .

For a porous medium of arbitrary permeability  $k$ , we can also write  $S_w^{\text{opt}} - S_w^{\text{min}} = P_c^{-1}(\Pi^-) - P_c^{-1}(\Pi^+)$  that is also equal to  $\pi/\Theta$ . From these two equalities, we infer the scaling relationship as follows:

$$\frac{S_w^{\text{opt}} - S_w^{\text{min}}}{(S_w^{\text{opt}})_{\text{ref}} - (S_w^{\text{min}})_{\text{ref}}} = \frac{\Theta_{\text{ref}}}{\Theta} = \frac{P_c^{-1}(\Pi^-) - P_c^{-1}(\Pi^+)}{P_{c,\text{ref}}^{-1}(\Pi^-) - P_{c,\text{ref}}^{-1}(\Pi^+)}.$$

That is:

$$\Theta = \Theta_{\text{ref}} \frac{P_{c,\text{ref}}^{-1}(\Pi^-) - P_{c,\text{ref}}^{-1}(\Pi^+)}{P_c^{-1}(\Pi^-) - P_c^{-1}(\Pi^+)}.$$

If one considers a narrow disjoining pressure interval, then the variation of inverse  $P_c$  and  $P_{c,\text{ref}}$  functions over  $\Pi$  interval can be respectively approximated as  $P_c^{-1}(\Pi^-) - P_c^{-1}(\Pi^+) = S_w^{\text{opt}} - S_w^{\text{min}} \approx \left(\frac{dS_w}{dP_c}\right)_{\Pi} (\Pi^- - \Pi^+)$  and  $P_{c,\text{ref}}^{-1}(\Pi^-) - P_{c,\text{ref}}^{-1}(\Pi^+) = (S_w^{\text{opt}})_{\text{ref}} - (S_w^{\text{min}})_{\text{ref}} \approx \left(\frac{dS_w}{dP_{c,\text{ref}}}\right)_{\Pi} (\Pi^- - \Pi^+)$ . This leads to:

$$\Theta = \Theta_{\text{ref}} \frac{\left(\frac{dS_w}{dP_{c,\text{ref}}}\right)_{\Pi}}{\left(\frac{dS_w}{dP_c}\right)_{\Pi}}.$$

That evolution of  $\Theta$  as a function of  $k$  cannot be predicted a priori from this relationship, even for homothetic porous media, because it depends on the shape of the  $P_c$  and  $P_{c,\text{ref}}$  curves with respect to the value of  $\Pi$ .

Considering now the *dynamic assumption*, the collapse of foam films occurs over an invariant interval of the transverse velocity gradient within pores, denoted  $[w'_{\text{max}}^-, w'_{\text{max}}^+]$ . As explained before, to that fixed transverse velocity interval correspond a pressure gradient interval  $[2\mu w'_{\text{max}}^-/r, 2\mu w'_{\text{max}}^+/r]$  along flow direction and a critical capillary pressure interval  $[P_c^{*-}, P_c^{*+}]$  for a porous medium with given characteristic pore radius  $r$  and permeability  $k$  ( $r \sim \sqrt{k}$ ). The invariance of  $[w'_{\text{max}}^-, w'_{\text{max}}^+]$  interval for different porous media implies that the interval  $[rP_c^{*-}, rP_c^{*+}]$  is constant since the pressure gradient and capillary pressure are in proportion one another. The scaling relationship for coalescence interval can then be expressed as an invariance of the product  $rP_c^*$  that we develop hereafter.

For two porous media with respective characteristic pore radii  $r$  and  $r_{\text{ref}}$ , the scaling relationship can be written over  $[w'_{\text{max}}^-, w'_{\text{max}}^+]$  interval as  $rP_c(S_w^{\text{opt}}) = r_{\text{ref}}P_{c,\text{ref}}[(S_w^{\text{opt}})_{\text{ref}}]$  and  $rP_c(S_w^{\text{min}}) = r_{\text{ref}}P_{c,\text{ref}}[(S_w^{\text{min}})_{\text{ref}}]$ , that is:

$$r \left[ P_c(S_w^{\text{opt}}) - P_c(S_w^{\text{min}}) \right] = r_{\text{ref}} \left[ P_{c,\text{ref}}((S_w^{\text{opt}})_{\text{ref}}) - P_{c,\text{ref}}((S_w^{\text{min}})_{\text{ref}}) \right].$$

For a generally-abrupt transition, previous relationship can be written:

$$r \left( S_w^{\text{opt}} - S_w^{\text{min}} \right) \left( \frac{dP_c}{dS_w} \right)_{S_w^*} = r_{\text{ref}} \left[ (S_w^{\text{opt}})_{\text{ref}} - (S_w^{\text{min}})_{\text{ref}} \right] \left( \frac{dP_{c,\text{ref}}}{dS_w} \right)_{(S_w^*)_{\text{ref}}}.$$

Taking into account the relationship established above between  $\Theta$  and saturation interval (Eq. 28), we infer the following general relation between  $\Theta$  and  $\Theta_{\text{ref}}$  that holds for any couple of porous media:

$$\Theta = \Theta_{\text{ref}} \frac{(S_w^{\text{opt}})_{\text{ref}} - (S_w^{\text{min}})_{\text{ref}}}{S_w^{\text{opt}} - S_w^{\text{min}}} = \Theta_{\text{ref}} \frac{r \left( \frac{dP_c}{dS_w} \right)_{S_w^*}}{r_{\text{ref}} \left( \frac{dP_{c,\text{ref}}}{dS_w} \right)_{(S_w^*)_{\text{ref}}}}.$$

For two homothetic porous media of characteristic pore radii  $r$  and  $r_{\text{ref}}$ ,  $P_c(S_w) = \frac{r_{\text{ref}}}{r} P_{c,\text{ref}}(S_w)$ , then the invariance of  $rP_c^*$ , i.e.  $rP_c(S_w^*) = r_{\text{ref}}P_{c,\text{ref}}[(S_w^*)_{\text{ref}}]$ , implies that  $P_{c,\text{ref}}(S_w^*) = P_c[\frac{r_{\text{ref}}}{r}(S_w^*)_{\text{ref}}]$ , i.e. that  $S_w^* = (S_w^*)_{\text{ref}}$ , which is also verified for the optimal and minimal saturation. Hence  $S_w^{\text{opt}} - S_w^{\text{min}} = (S_w^{\text{opt}})_{\text{ref}} - (S_w^{\text{min}})_{\text{ref}}$  and  $\Theta = \Theta_{\text{ref}}$ .

To end with, the transition saturation interval and the transition parameter  $\Theta$  are invariant for homothetic porous media under dynamic assumption.

## References

1. D. G. Bond and O. C. Holbrook. Gas drive oil recovery. Patent no. US Pat 2866507, 1958.
2. L. W. Holm. Foam injection test in the Siggins field, Illinois. *Society of Petroleum Engineers*, 22, 1970.

3. T. M. Jonas, S. I. Chou, and S. L. Vasicek. Evaluation of a CO<sub>2</sub> foam field trial: Rangely Weber Sand Unit. *Society of Petroleum Engineers*, 1990.
4. J. P. Heller, D. A. Boone, and R. J. Watts. Field test of CO<sub>2</sub> mobility control at Rock Creek. *Society of Petroleum Engineers*, Paper SPE-14395-MS, 1995.
5. J. J. Sheng. Foams and their applications in enhancing oil recovery. In *Enhanced Oil Recovery Field Case Studies*, pages 251–280. Elsevier, 2013.
6. A. R. Kovscek and C. J. Radke. Fundamentals of foam transport in porous media. in *Foams: fundamentals and applications in the petroleum industry*, American Chemical Society Advances in Chemistry (M. J. Comstock and L. L. Schramm Eds), 1994.
7. J. M. Alvarez, H. J. Rivas, and W. R. Rossen. Unified model for steady-state foam behavior at high and low foam qualities. *SPE Journal*, 6(3):325–333, 2001.
8. M. Lotfollahi, R. Farajzadeh, M. Delshad, A. Varavei, and W. R. Rossen. Comparison of implicit-texture and population-balance foam models. *Journal of Natural Gas Science and Engineering*, 31:184–197, 2016.
9. G. Bernard and W. L. Jacobs. Effect of foam on trapped gas saturation and on permeability of porous media to water. *Society of Petroleum Engineers Journal*, 5(04):295–300, 1965.
10. J. B. Lawson and J. Reisberg. Alternate slugs of gas and dilute surfactant for mobility control during chemical flooding. In *SPE/DOE Enhanced Oil Recovery Symposium*, 1980.
11. F. Friedmann, W. H. Chen, and P. A. Gauglitz. Experimental and simulation study of high-temperature foam displacement in porous media. *SPE Reservoir Engineering*, 6(01):37–45, 1991.
12. G. J. Hirasaki and J. B. Lawson. Mechanisms of foam flow in porous media: apparent viscosity in smooth capillaries. *Society of Petroleum Engineers Journal*, 25(02):176–190, 1985.
13. A. H. Falls, G. J. Hirasaki, T. W. Patzek, D. A. Gauglitz, D. D. Miller, and T. Ratulowski. Development of a mechanistic foam simulator: the population balance and generation by snap-off. *SPE Reservoir Engineering*, 3(03):884–892, 1988.
14. A. R. Kovscek, T. W. Patzek, and C. J. Radke. A mechanistic population balance model for transient and steady-state foam flow in Boise sandstone. *Chemical Engineering Science*, 50(23):3783–3799, 1995.
15. W. R. Rossen and P. A. Gauglitz. Percolation theory of creation and mobilization of foams in porous media. *AIChE Journal*, 36(8):1176–1188, 1990.
16. Z. F. Dholkawala, H. K. Sarma, and S. I. Kam. Application of fractional flow theory to foams in porous media. *Journal of Petroleum Science and Engineering*, 57(1-2):152–165, 2007.
17. P. A. Gauglitz, F. Friedmann, S. I. Kam, and W. R. Rossen. Foam generation in homogeneous porous media. *Chemical Engineering Science*, 57(19):4037–4052, 2002.
18. M. Lotfollahi, I. Kim, M. R. Beygi, A. J. Worthen, C. Huh, K. P. Johnston, M. F. Wheeler, and D. A. DiCarlo. Foam generation hysteresis in porous media: experiments and new insights. *Transport in Porous Media*, 116(2):687–703, 2017.
19. W. T. Osterloh and M. J. Jante. Effects of gas and liquid velocity on steady-state foam flow at high temperature. *Society of Petroleum Engineers*, (SPE/DOE 24179), 1992.
20. Z. I. Khatib, G. J. Hirasaki, and A. H. Falls. Effects of capillary pressure on coalescence and phase mobilities in foams flowing through porous media. *SPE Reservoir Engineering*, 3(3):919–926, 1988.
21. R. Farajzadeh, M. Lotfollahi, A. A. Eftekhari, W. R. Rossen, and G. J. H. Hirasaki. Effect of permeability on implicit-texture foam model parameters and the limiting capillary pressure. *Energy & Fuels*, 29(5):3011–3018, 2015.
22. R. A. Ettinger and C. J. Radke. Influence of texture on steady foam flow in Berea sandstone. *SPE Reservoir Engineering*, 7(1):83–90, 1992.
23. A. R. Kovscek and H. J. Bertin. Foam mobility in heterogeneous porous media. *Transport in Porous Media*, 52(1):37–49, 2003.
24. Q. Chen, A. R. Kovscek, and M. Gerritsen. Modeling foam displacement with the local-equilibrium approximation: theory and experimental verification. *SPE Journal*, 15(01):171–183, 2010.
25. H. Martinsen and F. Vassenden. Foam assisted water alternating gas (FAWAG) process on Snorre. *10<sup>th</sup> European Symposium on Improved Oil Recovery*, Brighton, UK, 1999.
26. L. Cheng, A. B. Reme, D. Shan, D. A. Coombe, and W. R. Rossen. Simulating foam processes at high and low foam qualities. *SPE/DOE Improved Oil Recovery Symposium*, Tulsa, Oklahoma, 2000.
27. S. I. Kam, Q. P. Nguyen, Q. Li, and W. R. Rossen. Dynamic simulations with an improved model for foam generation. *SPE Journal*, 12(01):35–48, 2007.
28. O. Gassara, F. Douarche, B. Braconnier, and B. Bourbiaux. Equivalence between semi-empirical and population-balance foam models. *Transport in Porous Media*, 120(3):473–493, Dec 2017.
29. C. S. Boeije and W. R. Rossen. Fitting foam-simulation-model parameters to data: I. coinjection of gas and liquid. *SPE Reservoir Evaluation & Engineering*, 18(02):264–272, 2015.
30. K. Ma, J. L. Lopez-Salinas, M. C. Puerto, C. A. Miller, S. L. Biswal, and G. J. Hirasaki. Estimation of parameters for the simulation of foam flow through porous media. part 1: the dry-out effect. *Energy & Fuels*, 27(5):2363–2375, 2013.

31. K. Ma, R. Farajzadeh, J. L. Lopez-Salinas, C. A. Miller, S. L. Biswal, and G. J. Hirasaki. Non-uniqueness, numerical artifacts, and parameter sensitivity in simulating steady-state and transient foam flow through porous media. Transport in Porous Media, 102(3):325–348, 2014.
32. F. P. Bretherton. The motion of long bubbles in tubes. Journal of Fluid Mechanics, 10(2):166, 1961.
33. O. Gassara, F. Douarache, B. Braconnier, and B. Bourbiaux. Calibrating and interpreting implicit-texture models of foam flow through porous media of different permeabilities. Journal of Petroleum Science and Engineering, 159:588–602, 09 2017.
34. D. W. Peaceman. Fundamentals of numerical reservoir simulation, volume 6 of Developments in Petroleum Science. Elsevier Science, Amsterdam, 1977.
35. J. A. Trangenstein and J. B. Bell. Mathematical structure of the black-oil model for petroleum reservoir simulation. SIAM J. Appl. Math., 49(3):749–783, 1989.
36. L. W. Lake. Enhanced oil recovery. Prentice Hall, 1989.
37. D. W. Green and G. P. Willhite. Enhanced oil recovery, volume 6 of SPE Textbook Series. Henry L. Doherty Memorial Fund of AIME, Society of Petroleum Engineers, 1998.
38. C. M. Marle. Multiphase flow in porous media. Gulf Publishing Company, third edition, 1981.
39. T. W. Patzek. Description of foam flow in porous media by the population balance method. in Surfactant-based mobility control, American Chemical Society Symposium Series (H. S. Duane Ed.), 1988.
40. S. I. Kam. Improved mechanistic foam simulation with foam catastrophe theory. Colloids and Surfaces A: Physicochemical and Engineering Aspects, 318(1-3):62–77, 2008.
41. A. Moradi-Araghi, E. L. Johnston, D. R. Zornes, and K. J. Harpole. Laboratory evaluation of surfactants for CO<sub>2</sub>-foam applications at the South Cowden Unit. International Symposium on Oilfield Chemistry, Houston, Texas, 1997.
42. F.A.L. Dullien. Porous Media: Fluid Transport and Pore Structure. Academic Press, second edition, 1992.
43. L. Pedroni and L. Nabzar. New insights on foam rheology in porous media. Rio Oil and Gas Expo and Conference 2016 Proceedings, (IBP. ISSN 2525 7560), 2016.
44. Z. Zhou and W. R. Rossen. Applying fractional flow theory to foam processes at the limiting capillary pressure. SPE Advanced Technology Series, 3(01):154–162, 1995.
45. V. Bergeron and C. J. Radke. Equilibrium measurements of oscillatory disjoining pressures in aqueous foam films. Langmuir, 8(12):3020–3026, 1992.
46. L. Kapetas, S. Vincent-Bonnieu, R. Farajzadeh, A. A. Eftekhari, S. R. Mohd-Shafian, R. Z. Kamarul Bahrim, and W. R. Rossen. Effect of permeability on foam-model parameters - an integrated approach from coreflood experiments through to foam diversion calculations. 18<sup>th</sup> European Symposium on Improved Oil Recovery, Dresden, 14-16 April, 2015.
47. R. H. Brooks and T. Corey. Properties of porous media affecting fluid flow. Journal of the Irrigation and Drainage Division, IR2(Proceedings of the American Society of Civil Engineers), 1966.
48. W. R. Rossen and Z. H. Zhou. Modeling foam mobility at the limiting capillary pressure. SPE Advanced Technology Series, 3(01):146–153, 1995.
49. H.-L. Chen, M.-J. Ke, T.-K. Chuang, and R. W. Flumerfelt. Experimental studies of capillary pressure effects of foams in porous media. SPE paper 20069, 1990.